Bioactive Materials 18 (2022) 354–367

Contents lists available at ScienceDirect

Bioactive Materials

journal homepage: www.keaipublishing.com/en/journals/bioactive-materials

Construction of a magnesium hydroxide/graphene oxide/hydroxyapatite composite coating on Mg–Ca–Zn–Ag alloy to inhibit bacterial infection and promote bone regeneration

Bo Yuan [a,b], Hewei Chen [a,b], Rui Zhao [a,b], Xuangeng Deng [c], Guo Chen [c], Xiao Yang [a,b], Zhanwen Xiao [a,b], Antoniac Aurora [d], Bita Ana Iulia [d], Kai Zhang [a,b], Xiangdong Zhu [a,b,*], Antoniac Vasile Iulian [d,e,**], Shen Hai [c,***], Xingdong Zhang [a,b]

[a] National Engineering Research Center for Biomaterials, Sichuan University, Chengdu, 610064, China
[b] College of Biomedical Engineering, Sichuan University, Chengdu, 610064, China
[c] Sichuan Provincial Orthopedic Hospital, Chengdu, 610041, China
[d] Faculty of Materials Science and Engineering, University Politehnica of Bucharest, 060042, Bucharest, Romania
[e] Academy of Romanian Scientists, 050094, Bucharest, Romania

ARTICLE INFO

Keywords:
Mg alloy
Composite coating
Corrosion resistance
Antibacterial ability
Osteogenic activity

ABSTRACT

The improved corrosion resistance, osteogenic activity, and antibacterial ability are the key factors for promoting the large-scale clinical application of magnesium (Mg)-based implants. In the present study, a novel nanocomposite coating composed of inner magnesium hydroxide, middle graphene oxide, and outer hydroxyapatite ($Mg(OH)_2$/GO/HA) is constructed on the surface of Mg-0.8Ca–5Zn-1.5Ag by a combined strategy of hydrothermal treatment, electrophoretic deposition, and electrochemical deposition. The results of material characterization and electrochemical corrosion test showed that all the three coatings have high bonding strength, hydrophilicity and corrosion resistance. *In vitro* studies show that $Mg(OH)_2$ indeed improves the antibacterial activity of the substrate. The next GO and GO/HA coating procedures both promote the osteogenic differentiation of MC3T3-E1 cells and show no harm to the antibacterial activity of $Mg(OH)_2$ coating, but the latter exhibits the best promoting effect. *In vivo* studies demonstrate that the Mg alloy with the composite coating not only ameliorates osteolysis induced by bacterial invasion but also promotes bone regeneration under both normal and infected conditions. The current study provides a promising surface modification strategy for developing multifunctional Mg-based implants with good corrosion resistance, antibacterial ability and osteogenic activity to enlarge their biomedical applications.

1. Introduction

As a new generation of medical metallic materials, magnesium (Mg) and its alloys have drawn substantial attention due to their biodegradability and closed elastic modulus to natural cortical bone [1,2]. Compared to conventional permanent metal implants, such as stainless steel, titanium, and titanium alloys, Mg-based implants could avoid the drawbacks of second operation and stress-shielding [3,4]. More importantly, recent many studies have demonstrated that Mg ions could facilitate bone regeneration and accelerate fracture healing by regulating bone biomineralization and formation of a pro-osteogenic immune microenvironment [5–7]. However, the fast degradation of Mg-based implants under physiological conditions would produce a large amount of hydrogen and induce an exponential decrease of the implant mechanical strength, resulting in impaired bone healing and failure of internal fixation [8,9]. In addition, bacteria might adhere and colonize on the surface of implants during tissue repair, which would rapidly proliferate and form eventually a dense bacterial film to greatly

Peer review under responsibility of KeAi Communications Co., Ltd.
* Corresponding author. National Engineering Research Center for Biomaterials, Sichuan University, Chengdu, 610064, China.
** Corresponding author. Faculty of Materials Science and Engineering, University Politehnica of Bucharest, 060042, Bucharest, Romania.
*** Corresponding author.
E-mail addresses: zhu_xd1973@scu.edu.cn (X. Zhu), antoniac.iulian@gmail.com (A.V. Iulian), shenhai_scsgkyy@163.com (S. Hai).

https://doi.org/10.1016/j.bioactmat.2022.02.030
Received 26 January 2022; Received in revised form 20 February 2022; Accepted 24 February 2022
Available online 3 March 2022

inhibit the killing effect of antibiotics and block subsequent osteogenesis, and thus leading to implant failure [10,11]. Hence, developing multifunctional Mg-based implants with good corrosion resistance, antibacterial ability and osteogenic activity is highly desirable to meet complex clinical needs.

To address this concern, performance optimization on biomedical Mg metals has been investigated extensively up to now, which was mainly based on the introduction of various metal ions via alloying treatment and construction of surface coatings via physical or chemical methods [12–15]. Some previous studies have demonstrated that alloying treatment alone was hard to meet the requirement of corrosion resistance and might weaken the inherent antibacterial performance of Mg alloys [16,17]. Compared to alloying treatment, fabricating protective coatings on Mg alloy surface can not only increase its corrosion resistance by isolating or decreasing the contacting surface area of the substrate with body fluid, but also endow it with some extraordinary biological functions [18–20]. For example, Chen et al. constructed a zoledronate-loaded coating on AZ31 Mg alloy via a combination strategy of fluoride pretreatment and dip coating to enhance its corrosion resistance as well as improve its osteogenic ability [21]. In addition, Wang et al. prepared a $Mg(OH)_2$ nanoflake coating in situ on the surface of pure Mg by an alkali-heat treatment, which significantly enhanced the corrosion resistance and antibacterial ability of the substrate material [22]. Among these protective coatings, calcium phosphate (CaP)-based coatings with similar chemical composition to the inorganic component of natural bone tissue are the most commonly used and investigated bioactive coating to improve the anti-corrosion property of Mg alloys [23,24]. In a recent clinical study, Xie et al. evaluated the effectiveness and safety of MgNdZnZr alloys with a CaP coating for the treatment of medial malleolar fractures [25]. Their results showed that the treatment of medial malleoli using modified Mg alloys screws achieved good functional recovery and fracture reduction [25], indicating excellent prospects for clinical translation. However, some previous studies indicated that fragility and weak bonding to the substrate of the coating potentially led to early failure of the bone-implant interface [26]. One possible approach to address this issue is to construct a composite coating with higher bonding strength by introducing a reinforced layer within the CaP coating.

Graphene oxide (GO) is considered an ideal nanoscale filler for the reinforcement of surface coatings due to its unique two-dimensional network structure, abundant chemical functional groups, and large specific surface area [27–29]. Recently, Wu et al. reported that rGO-reinforced apatite composite layers formed by hydrothermal treatment could enhance the apatite-substrate bonding strength and reduce the corrosion rate of AZ31 alloys [30]. More importantly, it was widely demonstrated that GO can not only directly mediate cell adhesion, proliferation, and differentiation by promoting fibronectin extracellular protein adsorption and enriching various growth factors in body fluids but can also cause physical and chemical damage to bacteria by strong surface tension and oxidative stress [31,32]. Thus, a combination of $Mg(OH)_2$, CaP, and GO may be a suitable way to construct a functional composite coating with excellent corrosion resistance, osteogenic activity, and antibacterial ability on the surface of Mg alloys. However, to our knowledge, construction of $Mg(OH)_2$/GO/CaP composite coatings on Mg alloys has never been reported.

In our previous study, we have prepared three MgCaZnAg alloys, including Mg-0.8Ca (ZQ), Mg-0.8Ca–5Zn-1.5Ag (ZQ71), and Mg-0.8Ca–5Zn-2.5Ag (ZQ63), by alloying with calcium (Ca), zinc (Zn), and silver (Ag) and evaluated their degradation behavior, biocompatibility, and antibacterial performance [17]. Our results showed that the introduction of Zn and Ag could partly enhance the corrosion resistance and osteogenic activity of Mg alloys but slightly weaken their initial inhibitory capacity against *Escherichia coli* (*E. coli*). Therefore, the aim of the present study was to modify the surface of Mg alloys to further enhance their corrosion resistance, osteogenic activity, and antibacterial ability. First, we selected a ZQ71 alloy with optimal performance as the target material and fabricated a $Mg(OH)_2$ coating in situ on its surface (named as ZQ71-H) by hydrothermal treatment using a sodium hydroxide (NaOH) solution. Second, electrophoretic deposition was applied to produce a GO layer on the ZQ71-H surface (named as ZQ71-HE), which provided multiple nucleation sites for the self-assembly of hydroxyapatite (HA). Finally, a HA composite coating was constructed on the surface of ZQ71-HE by electrochemical deposition (named as ZQ71-HEP). The degradation, biocompatibility, and antibacterial properties of the surface-modified Mg alloys were comprehensively evaluated *in vitro*. The *in vivo* osteogenic performances of them under infection and normal physiological conditions were investigated in detail using an infectious and/or normal bone defect model in rat femoral condyles.

2. Materials and methods

2.1. Sample preparation

ZQ71 alloy bulk was prepared by a melt-casting method [17] and mechanically machined into thin slices with dimensions of $10 \times 10 \times 1$ mm^3 for material characterization and *in vitro* study and cylinder with dimensions of $\Phi 3 \times 4$ mm^3 for *in vivo* animal study. After cleaning and drying, the samples were put into a 25 mL autoclave containing 10 mL of NaOH (pH = 12) and treated hydrothermally in an oven at 120 °C (ZQ71-H) for 12 h. After hydrothermal treatment, the autoclave was cooled in air, and the samples were ultrasonically cleaned with deionized water and dried in nitrogen for subsequent electrophoretic deposition.

An electrochemical workstation (PARSTAT 2273, Princeton Applied Research, USA) was used to electrophoretic deposition on the surface of ZQ71-H. Isopropanol and aluminum nitrate were used as the dispersant and electrolyte, respectively, for the configuration of the GO deposition solution. A constant current/voltage (0.1 A/120 V) was applied to the ZQ71-H sample for 20 min (ZQ71-HE), where the Mg alloy and ring-shaped graphite electrode were utilized as the cathode and anode, respectively. After electrophoretic deposition, pulse electrochemical deposition was performed on the ZQ71-HE sample using the PARSTAT 2273 workstation, where a pulsed current (0 V, 10 s; 24 V, 1 s) was applied to the sample being immersed in an electrolyte at 80 °C for 100 cycles. The as-deposited sample was then cleaned with deionized water and dried to obtain the ZQ71-HEP sample.

2.2. Material characterization

A field-emission scanning electron microscopy (FE-SEM, S4800, Hitachi, Japan) equipped with an energy dispersive spectrometry (EDS) was used to examined the surface morphologies and elemental composition. The surface nanotopography and roughness of the samples were further evaluated by an atomic force microscope (AFM, Asylum Research, MFP-3D, USA). A water contact angle measurement machine (lL4200, KRÜSS GmbH, Germany) was utilized to detect the wettability of the samples, where parallel tests were carried out on three non-overlapping areas of each sample. Phase composition of the samples was determined by X-ray diffractometer (XRD, DX-1000, China). An fourier transform infrared spectrophotometer (FTIR, Nicolet 6700, Thermo Fisher Scientific, USA) was used to investigate the surface chemical groups of the samples. The bonding strength of the coating was evaluated by using a microscratch tester (MST, Anton Paar GmbH, Germany). A spherical diamond tip of 100 μm radius with a progressive load from 0 to 10 N was used.

2.3. Electrochemical corrosion tests

The PARSTAT 2273 electrochemical workstation was utilized to perform the electrochemical corrosion tests, including open circuit potential (OCP), electrochemical impedance spectroscopy (EIS) and

potentiodynamic polarization (PDP). A standard three-electrode system was used in the electrochemical measurements, in which a saturated calomel electrode (SCE) and a hollow graphite cylinder were utilized as the reference electrode and counter electrode, respectively. The EIS tests were conducted at an open circuit potential with an applied AC signal of amplitude 10 mV from 100 kHz to 0.1 Hz. Over a potential range of −2.2 V–0.6 V, the PDP curves were obtained at a scan rate of 1.67 mV s^{-1}. In EIS and PDP tests, a PBS solution composed of 8.1 mM Na_2HPO_4, 1.9 mM NaH_2PO_4, and 145 mM NaCl with pH 7.2–7.4 was used. All tests were repeated independently three times.

2.4. Immersion test

In order to further evaluate the long-term durability of the Mg alloy samples *in vitro*, the four samples were immersed in cell culture medium at 37 °C for 1, 4, 7 and 14 days to detect pH variation and weight loss. The immersion media was changed every two days.

2.5. Cell morphology and viability

Mouse MC3T3-E1 pre-osteoblasts were cultured with a-minimum essential medium (α-MEM, Gibco, USA) containing 10% (v/v) standard fetal bovine serum (FBS, Gibco, USA) and 1% (w/v) penicillin/streptomycin (Gibco, USA). The samples were sterilized by gamma radiation and placed in 24-well plates. After balancing the culturing environment for 12 h by 2 mL medium, MC3T3-E1 cells were seeded on each sample at a density of 1×10^4 cell per/well. The culture medium was changed every day. A confocal laser scanning microscope (CLSM, TCS-SP5, Leica Microsystems, Germany) was used to observe the morphology of MC3T3-E1 cells cultured on each sample. After 3 days of culture, the cells were stained with fluorescein diacetate (FDA, Sigma, USA) and propidiumiodide (PI, Sigma, USA). For visualize cytoskeleton and cell nucleus, the cells were stained with Phalloidin-TRITC (Sigma) and 4',6-Diamidino-2-phenylindole dihydrochloride (DAPI, Sigma). Cell counting kit-8 assay (CCK-8, Dojindo, Japan) was utilized to evaluate the viability of MC3T3-E1 cells co-cultured with each sample.

2.6. Osteogenic gene expression

After 11 days of culture, expression of osteogenic-related genes, including alkaline phosphatase (ALP), type I collagen (Col-I), osteocalcin (OCN), osteopontin (OPN), and osterix (OSX), in MC3T3-E1 cells was analyzed by real-time quantitative polymerase chain reaction (qRT-PCR, CFX96™ system, Bio-Rad, USA). Primer sequences of the genes are listed in Table S1. According to the manufacturer's specification, RNA of the cells was extracted using a RNeasy mini kit (Qiagen, Germany) and then transcribed into complementary DNA (cDNA) using an iScript cDNA Synthesis Kit (Bio-Rad, USA). Gene expression was quantified using qRT-PCR with Supremix (Transgen Biotech, China), and GAPDH was used as the housekeeping gene to normalize the data.

2.7. Antibacterial activity in vitro

The *in vitro* antibacterial properties of the Mg alloys was evaluated using *E. coli* and *Staphylococcus (S. aureus)*. *E. coli* and *S. aureus* were diluted to 6.21×10^4 CFU mL^{-1} and 6.39×10^4 CFU mL^{-1} with Luria-Bertani (LB) to culture with the Mg alloys, respectively. After culturing for 8, 12, 16 and 24 h, the absorbency of the culture medium was measured by a spectrophotometer (UNIC-7200, China) at 410 nm for *E. coli* and 650 nm for *S. aureus*. The morphology and structure of the bacterial cultured on the surface of the samples were observed by SEM after culturing for 12 h. For further observing the number of bacterial colonies cultured on the samples for 24 h, a 10 μL bacteria-containing medium were plated onto LB agar plates. After 24 h of culture, photos were taken.

2.8. Surgical procedure

All experimental procedures were approved by the Animal Ethics Committee of Sichuan University. Twenty-seven female Sprague-Dawley rats aged 8 weeks were purchased from the Animal Center of Sichuan University (Chengdu, China). All rats were divided into two groups to establish the normal models (9 rats) and infection models (18 rats). Taking into account the "3R principle" of anmial (ethics reduce, refine and replace) [33], herein only ZQ71-HEP with optimal performances was set as experimental group for the *in vivo* experiments to avoid unnecessary animal experiments. In the two models, ZQ71 was set as material control. In the normal models, the saline was used as blank control. In the infection models, polyetheretherketone (a bio-inert polymer) and bacteria liquid were used as negative control for antibacterial activity evaluation and blank control for osteogenesis evaluation, respectively.

A femoral condyle defect model was established in each rat according to our previous work [34]. Briefly, the rats were anaesthetized with intraperitoneal injection of pentobarbital (Nembutal 2 mg/100 g). After skin incision, the femoral condyle was exposed by blunt dissection. A cylindrical hole with 3 mm diameter and 4 mm depth was created perpendicular to the distal femur of rats using a dental drill. The normal femoral condyle defects were generated and the sample was directly implanted into the hole. 10 μL of *S. aureus* (1×10^7 CFU mL^{-1}) was injected into the hole carefully and slowly using 10 μL pipette to establish the infection models. To prevent bacterial suspension leakage, the pipette was taken out 20 s later and the sample was implanted. For *in vivo* fluorescent labeling, the rats were injected intraperitoneally with tetracycline (30 mg/kg body weight, Sigma) at 14 days and calcein (6 mg/kg body weight, Sigma) at 4 days, respectively, before euthanasia.

2.9. Antibacterial activity evaluation

At 7 days postoperatively, 9 rats were randomly selected from the infection model and euthanized by intraperitoneal injection of an overdose of sodium pentobarbital. The complete blood was collected from the rats by a heart puncture for blood routine tests. The distal femur of rat was collected and the implanted sample was gently pulled out under aseptic conditions to evaluate the antibacterial activity. The implanted sample was ultrasonicated for 4 min in 4 mL PBS solution to isolate the bacteria. The isolated bacteria were diluted and cultured within LB agar plates, and incubation for 24 h at 37 °C to count the number of bacterial colonies. After sonication, the implanted samples were fixed in 2.5% glutaraldehyde for 12 h and dehydrated with graded alcohol for further SEM observation.

Histopathological examination was performed on the bone specimens to observe the inflammatory response around different implanted samples at 7 days. After fixing with paraformaldehyde for 24 h, the bone specimens were decalcified in ethylenediaminetetraacetic acid disodium solution for 4 weeks, followed by embedding in paraffin and cutting into ~5-μm-thick sections. Then, the sections were stained with HE, and Giemsa. The stained sections were observed and imaged using a light microscope (BX60, Olympus, USA).

2.10. Osteogenic activity evaluation

Four weeks after surgery, all rats were euthanized by intraperitoneal injection of an overdose of sodium pentobarbital. Blood was collected and serum was separated by centrifugation (4000 rpm for 15 min at 4 °C). The serum level of procollagen I N-terminal propeptide (PINP) was assayed using a rat PINP ELISA kit (Cloud-Clone Corp., USA) according to the manufacturer's specifications. A micro-computed tomography imaging system (μ-CT, SCANCO VivaCT 80, Switzerland) was used to evaluate the bone formation and observe the degradation of the samples at 4 weeks postoperatively. The newly formed bone from each implant was segmented using a global threshold during the

reconstruction, in which the degradation rates of implants were calculated as the degraded material volume (ΔMV) divided by the initial material volume (MV), and the new bone substitution rates were calculated as the bone volume (BV) divided by the ΔMV.

After μ-CT evaluation, the fixed bone specimens (n = 6) were dehydrated and then embedded in polymethylmethacrylate. A microtome (SAT-001, AoLiJing, China) was used to cut the embedded specimen into ~100 μm-thick sections. After grinding and polishing to a final thickness of ~25 μm, the sections were stained with H&E and observed by the light microscope. Using Image Pro Plus software (Media Cybernetic, USA), the acquired microscope images were histologically evaluated for quantitative analysis of newly formed bone. During the evaluation, the BA/ΔMA was calculated as the percentage area of degraded materials, and the BA/ΔMA was defined as the percentage area of bone substitution. In addition, the nonstained sections were observed by CLSM to evaluate the mineral apposition activity of new bone formation by monitoring the fluorescence intensity of tetracycline and calcein label.

2.11. Statistical analysis

All data are expressed as the mean ± standard deviation (SD) of three independent experiments, unless otherwise stated in the caption. Statistical analysis was carried out using SPSS 16.0 software, and one-way ANOVA with Tukey's post hoc test was performed to determine the significant differences between groups. Differences were considered statistically significant when p-values < 0.05.

3. Result and discussion

3.1. Preparation and characterization of $Mg(OH)_2$/GO/HA nanocomposite coating with high bonding strength

The $Mg(OH)_2$/GO/HA nanocomposite coating was constructed in situ on the ZQ71 substrate in three steps, as illustrated in Fig. 1A. Hydrothermal treatment was used to convert the smooth surface of Mg alloy into the $Mg(OH)_2$ nanosheets coating, as confirmed by SEM

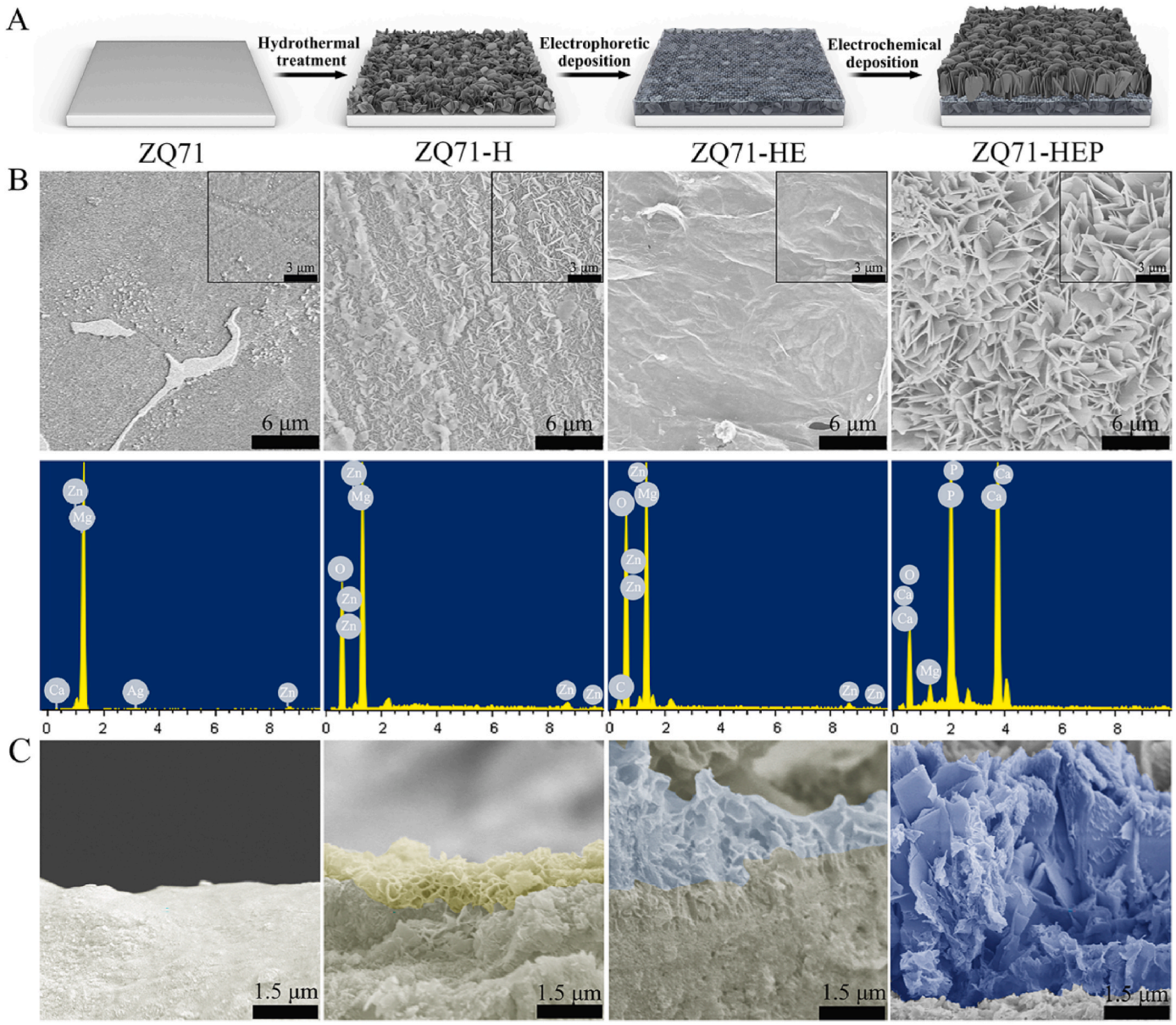

Fig. 1. Preparation and morphological characterization of various ZQ71 samples. (A) Schematic illustration of the preparation of various ZQ71 samples. (B) Surface SEM images and EDS analysis and (C) cross-section SEM images of various ZQ71 samples.

coupled with an EDS (Fig. 1B). After further electrophoretic deposition, a flocculent-lamellae GO film mainly consisting of C and O elements was introduced into the $Mg(OH)_2$ layer, which provided multiple nucleation sites for the self-assembly of HA nanosheets driven by the electrochemical deposition. From the cross-section images, the three-layered composite coating was crack-free and had a continuous interface (Fig. 1C), indicating a strong interfacial bonding. The surface coatings with nanoscale topographies and hydrophilic groups not only enhanced the average roughness of the modified ZQ71 samples but also improved their hydrophilicity (Fig. 2A–C), which was essential for good bioactivity [35]. It is worth noting that both ZQ71-H and ZQ71-HEP showed higher hydrophilicity than ZQ71-HE, as should be ascribed to the rough nanosheets on the former two samples [36]. To verify the chemical composition of the coatings, both FTIR and XRD analyses were performed on various ZQ71 samples. As shown in Fig. 2D, after hydrothermal treatment, an intense characteristic peak at 3696 cm^{-1} was observed in the spectra of ZQ71-H, which corresponded to Mg–OH [37]. Different from the spectra of ZQ71-H, the peak at 1730 cm^{-1} in the spectra of ZQ71-HE was assigned to the degenerate asymmetric C═O stretching vibration [38]. The peak at 1619 cm^{-1} was attributed to the symmetric C═C stretching vibration of the graphene skeleton. Compared to ZQ71-HE, there were some new characteristic peaks at approximately 1036 cm^{-1} and 964 cm^{-1} in the spectra of ZQ71-HEP, which were attributed to P–O stretching. According to the XRD patterns (Fig. 2E), the characteristic peaks of ZQ71 corresponded mainly to α-Mg, $Ca_2Mg_6Zn_3$, and Mg_3Ag [17]. The characteristic peaks of Mg $(OH)_2$ at 18.4° and 36.7° occurred on ZQ71-H after hydrothermal treatment [37]. Compared to ZQ71-H, a new characteristic peak at 10.2° in the pattern of ZQ71-HE corresponded to the reflection of GO [39]. After further electrochemical deposition, typical HA peaks (JCPDS 9-0432) were present on ZQ71-HEP [40].

The coating-substrate bonding strength is critical for osteointegration and the success of implant therapy [41]. The bonding force between the coating and Mg alloy substrate was determined by the microscratch test. As shown in Fig. S1, the acoustic emission signal and friction force as functions of loading force during the microscratch test showed that a weak peak in acoustic emission of the ZQ71-H occurred at ~1 N (L1), which might be associated to the formation of microcracks within the $Mg(OH)_2$ coating [42]. The number of microcracks increased with time and the microcracks were gradually merged to promote the formation of a macrocrack (i.e., fracturing), as confirmed by a series of characteristic peaks (L2-L3). As the critical stress distribution exceeded the coating thickness, the $Mg(OH)_2$ coating started delaminating and shedding (L3), resulting in the exposure of ZQ71 substrate with metallic lustre (bright white). Both ZQ71-HE and ZQ71-HEP showed similar acoustic emission signals and friction force to ZQ71-H, suggesting that there was no delamination between $Mg(OH)_2$ and GO or GO/HA coating at critical load. This also indicated that the bonding strength between $Mg(OH)_2$ and GO or GO/HA was significantly higher than that between $Mg(OH)_2$ and ZQ71 substrate. Different from the three samples, the acoustic emission signal of ZQ71 modified by $Mg(OH)_2$/HA coating (ZQ71-HP) showed an abrupt jump at 2.2 N, followed by continuous high-frequency characteristic peaks. The characteristic peaks of ZQ71-HP at 2.2 N and 2.7 N might be attributed to the delamination between $Mg(OH)_2$ and HA coating, and the shedding of $Mg(OH)_2$/HA composite coating [43], respectively. In conjunction with the scratch topography analysis, the

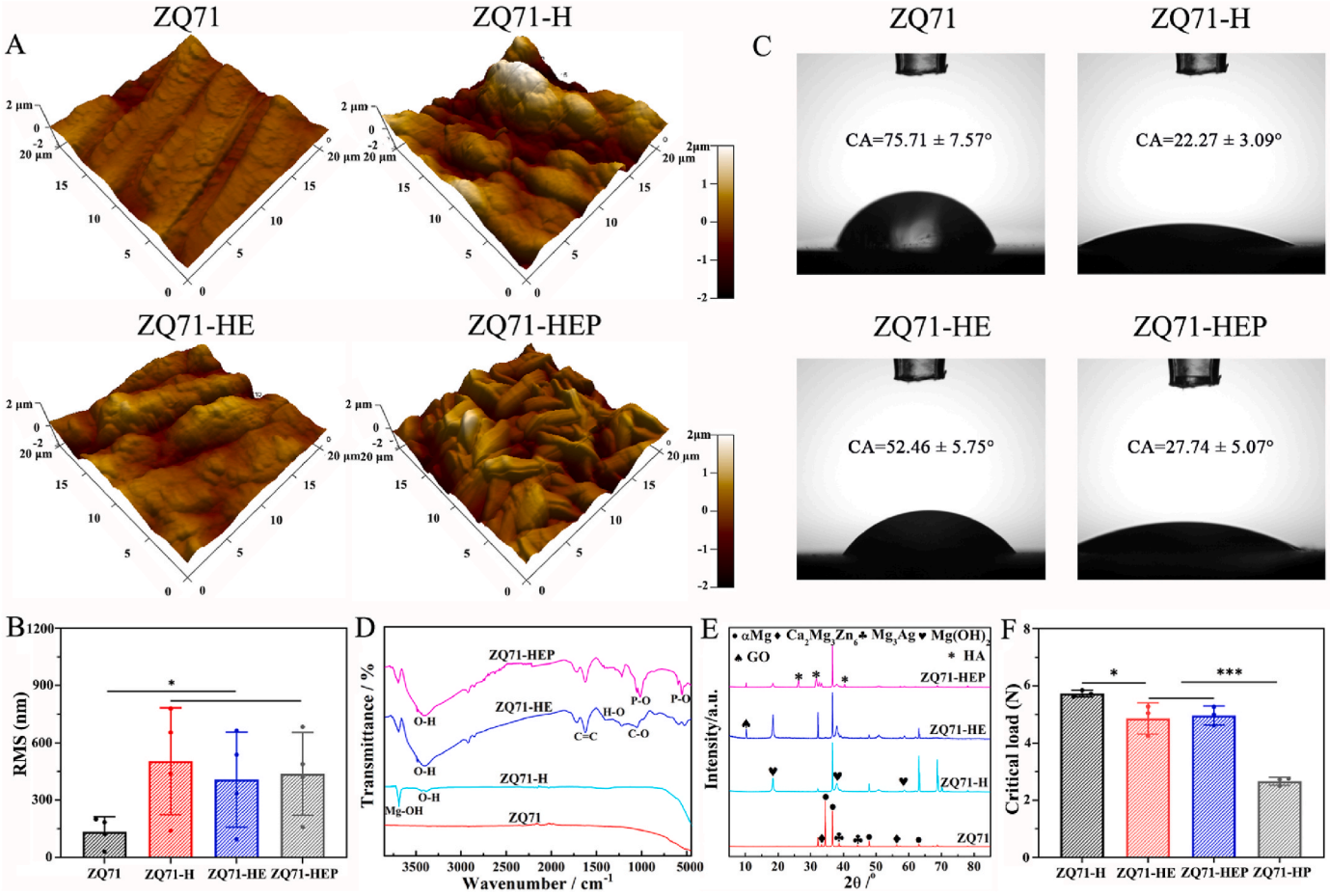

Fig. 2. Surface characterization of various ZQ71 samples. (A) Surface AFM images and (B) corresponding surface roughness of various ZQ71 samples. (C) The morphologies and contact angles of water droplets on the surface of various ZQ71 samples. (D) FTIR spectra and (E) XRD patterns of various ZQ71 samples. (F) Bonding strength of various coating. (*$p < 0.05$, **$p < 0.01$, ***$p < 0.001$).

bonding forces (L3) between the coating and the substrate on the four samples (ZQ71-H, ZQ71-HE, ZQ71-HEP, and ZQ71-HP) were 5.73 ± 0.12, 4.86 ± 0.54, 4.96 ± 0.33 and 2.67 ± 0.14 N, respectively (Fig. 2F). According to Hertz's theory [44], the critical contact pressure of Mg $(OH)_2$/GO/HA composite coating was estimated to be 5.81 ± 0.65 GPa, which could be compared with the hardness of natural bone [45]. The microscratch analysis showed that the introduction of GO coating could significantly enhance the bonding strength between $Mg(OH)_2$ and HA coating by the chemical bonding of abundant functional groups.

3.2. *$Mg(OH)_2$/GO/HA nanocomposite coating enhanced the corrosion resistance of ZQ71 alloy*

Surface modification of Mg alloys aims to construct an anti-corrosion layer with good surface biocompatibility on the surface of the substrate [26]. To evaluate the effects of different coatings on the corrosion resistance of ZQ71 substrates, electrochemical corrosion tests were performed in a PBS solution. As shown in Fig. 3A, after soaking in PBS for 900 s, the OCP of the four ZQ71 samples reached a stable state. Compared to the untreated ZQ71, the modified ZQ71 showed far higher OCP values, and the OCP in both ZQ71-H and ZQ71-HEP was significantly higher than that in ZQ71-HE, indicating a lower corrosion tendency and higher electrochemical stability [46]. The representative PDP curves showed that all ZQ71 samples presented similar polarization curves in terms of their shape (Fig. 3B), suggesting a similar corrosion behavior. For a quantitative comparison, a Tafel extrapolation was performed on the cathodic polarization curve to calculate the polarization parameters, including the corrosion potential (E_{corr}) and corrosion current density (i_{corr}) (Table S2). The results showed that the i_{corr} value for ZQ71-H and ZQ71-HEP decreased approximately two orders of magnitude compared to that of ZQ71, which was at least one order of magnitude lower than the lowest i_{corr} reported in some previous studies [37,45], demonstrating that the combination of alloying treatment and constructing composite coating can significantly enhance the corrosion resistance of Mg . In order to clarify the protection capability of various coatings, each i_{corr} value was used to calculated the corresponding corrosion protection efficiency (P_i) by using the following formula [47].

$$P_i(\%) = (1 - \frac{i_{corr}}{i^0_{corr}}) \times 100 \quad (1)$$

where i_{corr} and i^0_{corr} and denote the corrosion current densities of the surface-coated and uncoated samples, respectively. It is clear that the $Mg(OH)_2$ coating had the maximum protection efficiency followed by the $Mg(OH)_2$/GO/HA coating.

To trace the corrosion behavior of the four samples in PBS solution, the EIS measurements were performed at the open-circuit potential. The Nyquist plots in Fig. 3C show that all of these EIS loci look like an approximate line, whereas each may actually be a portion of a depressed semicircle with a giant diameter within the frequency range of analysis (see inserted image in Fig. 3C). In general, a semicircle in the Nyquist plots indicates multiple processes with similar relaxation time constants, which can be further identified by the Bode phase-angle plots [46]. As shown in Fig. 3D, all modified ZQ71 samples showed an approximate phase angle plateau, but a phase peak at 0.6 Hz occurred on the Bode phase-angle plot of untreated ZQ71, which may be associated with the dissolution of the Mg alloy. For these approximate phase angle plateaus, each plateau corresponded to a different phase value, representing a different capacitive response. In the low-frequency range, the following order of impedance modulus (|Z|) was observed: ZQ71-H (5.61×10^3 Ω cm^2) > ZQ71-HEP (2.87×10^3 Ω cm^2) > ZQ71-HE (5.24×10^2 Ω cm^2) > ZQ71 (80.48 Ω cm^2), indicating that the order of corrosion resistance is ZQ71-H > ZQ71-HEP > ZQ71-HE > ZQ71 (Fig. 3E). To further analyze the corrosion properties of the four alloys, the electrochemical reactions occurring on each sample was simulated by an electrochemical equivalent circuit model according to our previous study [17]. In the equivalent circuits, R_s denotes the sum of the solution resistance and Mg alloy surface resistance, R_f and Q_f are the resistance and capacitance of the inner film, respectively; R_g and Q_g are the bilayer resistance and capacitance of the intermediate coating, respectively; R_h denotes the resistance of the outer layer; and L is the inductance formed by the adsorption of products. Moreover, a constant phase element (CPE) is used to replace the conventional capacitance element in the circuit.

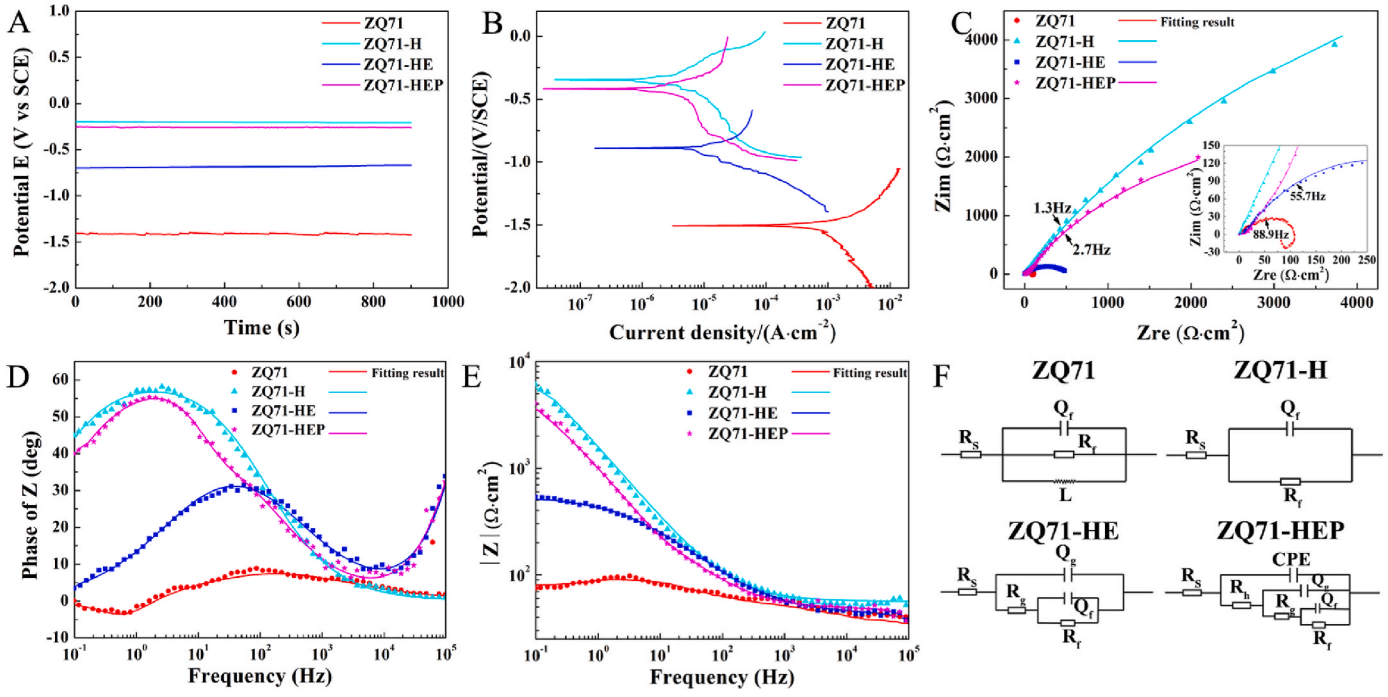

Fig. 3. Electrochemical testing results of various ZQ71 samples. (A) The open circuit potential, (B) Potentiodynamic polarization curves, (C) Nyquist plots, (D) Bode plots of phase angle vs. frequency, and (E) Bode plots of |Z| vs. frequency of various ZQ71 samples in PBS solution at 37 °C. (F) The electrochemical equivalent circuit model of various ZQ71 samples.

Using the commercial software ZsimpWin3.1, the EIS data were fitted to the equivalent circuit shown in Fig. 3F, and the fitted values are listed in Table S3. The order of R_f is ZQ71-H > ZQ71-HEP > ZQ71-HE > ZQ71, and the order of Q_f is ZQ71-H < ZQ71-HEP < ZQ71-HE < ZQ71. To compared the contribution of various coatings to corrosion protection of Mg alloy, the value of R_f listed in Table S3 was also used to calculate the protection efficiency (P_R) by the following formula [46].

$$P_R(\%) = (1 - \frac{R_f^0}{R_f}) \times 100 \quad (2)$$

where R_f and R_f^0 stand for the charge transfer resistance of the surface-coated and uncoated sample, respectively. Consistent with the results of PDP measurements, the corrosion protection efficiency based on R_f values showed that both $Mg(OH)_2$ and $Mg(OH)_2$/GO/HA coating markedly increased the protection efficiency of Mg alloy.

Considering that the electrochemical tests were instantaneous measurement, a long-term immersion test was carried out to further evaluate the corrosion resistance of the four samples. The results shown in Fig. S2A indicated that the pH value of the culture medium containing ZQ71 sample increased with the increasing of culture time, and then reached up to approximately 9.26 at 14 days, which was significantly higher than that of each modified group. In addition, ZQ71 exhibited greatest weight loss during the entire immersion period (Fig. S2B). Notably, ZQ71 presented a severe corrosion state after immersion for 14 days as its surface exhibited a rough and corroded morphology, on which numerous cracks and degradation products could be observed (Fig. S2C). No obvious morphology or structure change on each composite coating sample was found, indicating its good protective ability and long-term stability. The above results show that the coatings on the surface of ZQ71 effectively protected the substrate from defects and corrosion, and $Mg(OH)_2$ had a more significant protection effect.

In general, the introduction of impurities and alloying elements will

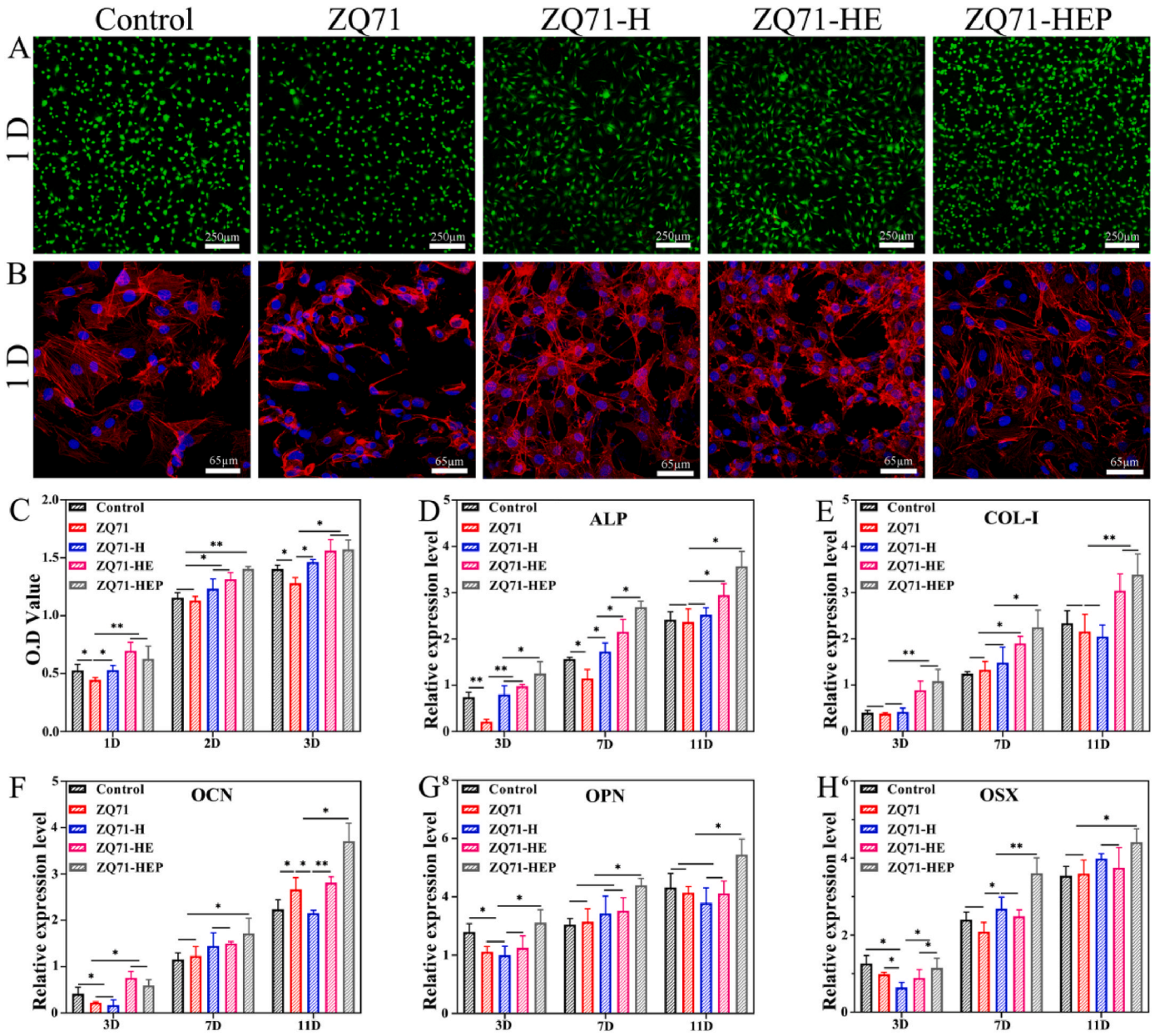

Fig. 4. *In vitro* cytocompatibility of various ZQ71 samples. (A) CLSM images of the cells stained by FDA and PI. (B) CLSM images of the cell cytoskeleton (red) and nucleus (blue) stained by rhodamine-phalloidin and DAPI. (C) Cell viability of MC3T3-E1 cultured with different ZQ71 samples at day 1, 2 and 3. (D–H) qRT-PCR analysis for several osteogenic gene expression of MC3T3-E1 cultured with different ZQ71 samples at day 3, 7 and 11. (*$p < 0.05$, **$p < 0.01$, ***$p < 0.001$)

result in the corrosion occurring in Mg alloys due to the galvanic corrosion formed between the active Mg matrix and other phases [48]. After hydrothermal treatment, a dense $Mg(OH)_2$ nanosheet layer with air pockets blocked electron transfer and protected the ZQ71 substrate underneath water and oxygen [22], thereby retarding its corrosion. However, unlike initial expectations, the GO layer degraded the corrosion protection of the $Mg(OH)_2$ layer instead of increasing after further electrophoretic deposition. The reason for this phenomenon may be associated with a variation in the properties of the $Mg(OH)_2$ layer, including the dielectric constant, chemical and physical defect density, due to the cathodic polarization and impurity ion adsorption occurring on the surface of ZQ71-HE driven by a high voltage during electrophoretic deposition [44]. In contrast, electrochemical deposition of HA at low voltage avoided impurity ion adsorption and strengthened the protective effect of the composite coating.

3.3. $Mg(OH)_2$/GO/HA nanocomposite coating promoted osteogenic differentiation of MC3T3-E1 cells

To evaluate the effects of different coatings on the potential bone-formation ability of ZQ71, we cultured them with MC3T3-E1 pre-osteoblasts. Fig. 4A shows representative fluorescence microscopy images of MC3T3-E1 cells cultured on different ZQ71 samples for 1 day. With increased culturing time, live cells on the surface of each sample increased prominently and presented a normal cell morphology (Fig. S3A), indicating good *in vitro* biocompatibility of the ZQ71 samples. After further staining for the cell cytoskeleton and nucleus, the spreading morphology of cells cultured on different samples was observed. As shown in Fig. 4B and Fig. S3B, greater cytoplasmic expansion and filamentous pseudopdia extension were observed in both the control and ZQ71-HEP groups compared with the other ZQ71 samples, as confirmed by the larger cell spreading area (Fig. S3C). The CCK-8 assay showed that both ZQ71-HE and ZQ71-HEP exhibited higher cell viability than the other groups (Fig. 4C), resulting in a higher cellular nuclei density (Fig. S3D). The enhanced cell spreading and viability could be attributed to the increased corrosion resistance, which significantly retarded the degradation of the substrate and created a relatively stable microenvironment for cell adhesion and growth [49], as well as the enhanced bioactivity of the GO/HA coating.

Furthermore, we investigated the effects on key osteogenic gene expression in MC3T3-E1 cells cultured with various ZQ71 samples (Fig. 4D–H). For ALP, an early stage osteogenesis marker [50], the gene expression in the untreated ZQ71 group was significantly lower than that in the control group at days 3 and 7, but no significant difference was observed between the control and ZQ71-H groups. For Col-I, both ZQ71-HE and ZQ71-HEP upregulated its gene expression compared to the other three groups throughout the culture period, but no significant difference in gene expression was found between ZQ71-HE and ZQ71-HEP or between the other three groups. For OCN, ZQ71-HEP consistently exhibited stronger effects on its gene expression than the other groups, and ZQ71-HE upregulated the gene expression of OCN at days 3 and 11. However, compared to the control group, no experimental group upregulated the gene expression of OPN except for ZQ71-HEP throughout the culture period. Similarly, for OSX, only ZQ71-HEP showed significantly higher gene expression than the control group at days 7 and 11. These results indicate that the construction of the $Mg(OH)_2$/GO/HA composite coating could have a positive effect on promoting the osteogenic differentiation of osteoblasts [41,51].

3.4. $Mg(OH)_2$/GO/HA nanocomposite coating enhanced the antibacterial activity of ZQ71 alloy

In addition to exploring the effect of different coatings on promoting cell osteogenesis, we also investigated whether the coatings enhanced the antibacterial properties of ZQ71. Consistent with our previous study, quantitative analysis of the antibacterial capacity after culturing for 24 h indicated that the antibacterial rates of ZQ71 against *S. aureus* and *E. coli* at 24 h were 80.5 ± 0.9 and 80.3 ± 1.5%, respectively (Fig. 5A and B), indicating that ZQ71 had good inherent antibacterial ability [17]. After hydrothermal treatment, the antibacterial capacity of ZQ71 with $Mg(OH)_2$ coating increased by a factor of 1.09–1.12. However, no significant difference in the antibacterial rates was observed among the three modified ZQ71 groups, suggesting that the GO and GO/HA coatings had a comparable antibacterial activity with $Mg(OH)_2$ coating.

The bacterial morphology and membrane integrity of the bacteria cultured on the samples were observed by SEM, and the results are shown in Fig. 5C. Generally, the *S. aureus* cells were spherical in shape with a smooth surface, and the *E. coli* cells had rod shapes with round ends. In this study, the bacterial cells for both *S. aureus* and *E. coli* attached loosely to the surface of the ZQ71 samples, and their surface was coarse and distorted. Compared to the intact bacterial membrane in ZQ71 group, cell membrane damage with leakage of intracellular material (dark arrow) was clearly observed in the ZQ71-H group, which was mainly due to the mechanical tension of $Mg(OH)_2$ nanosheet onto the bacteria membranes resulting in severe deformation of the membrane [22]. Similar bacterial morphology was also observed on the surface of ZQ71-HE, which should be ascribed to the membrane stress and superoxide anion-independent oxidative stress induced by the GO coating [52,53]. The HA coating on the surface of ZQ71-HEP had nano-scaled roughness and high hydrophilicity that might allow it to avoid the close contact of rigid cell wall of the bacteria and then reduced bacterial adhesion [54–57]. To verify the above results, an agar plate experiment was performed on different ZQ71 samples. By counting the bacterial colonies, we found that the *S. aureus* and *E. coli* colony numbers of the experimental groups were significantly reduced compared with those of the control group (Fig. 5D). After normalizing to ZQ71, no significant difference in the percent reduction of colonies was observed between the three surface-coated ZQ71 groups (Fig. S4). The above *in vitro* results demonstrate that three coating modified ZQ71 showed equivalent antibacterial activity *in vitro*, but ZQ71-HEP had a stronger ability to promote osteogenic differentiation than ZQ71-H and ZQ71-HE. Therefore, considering the "3R principle" of animal ethics, only ZQ71-HEP (but not ZQ71-H and ZQ71-HE) was selected as a candidate for further *in vivo* study.

To confirm the antibacterial activity of the modified ZQ71 surface *in vivo*, the samples were implanted into metaphyseal defects in infected rat femurs. During the first 7 days of implantation, we monitored the changes in body weight and white blood cells. No significant difference in body weight was found, whereas white blood cell counts (WBCs) differed greatly among the groups (Fig. S5 and Fig. 6A). Both ZQ71 and ZQ71-HEP showed far lower WBCs than the control group, and the WBC in ZQ71-HEP was significantly lower than that in ZQ71, indicating a weaker systemic inflammation [58]. By culturing the bacterial colonies derived from the implant surface, we found that the number of bacterial colonies on the surface of ZQ71 and ZQ71-HEP was significantly reduced compared to that on the control implant (Fig. 6B). According to the quantitative analysis of the bacteria colonizing the implant surface, construction of a $Mg(OH)_2$/GO/HA composite coating enhanced the antibacterial ability of the ZQ71 implant by ~145%. Further observation of the implant surface by SEM revealed bacteria encapsulated with biofilm-like compounds on the surface of the control implant but not on the surface of ZQ71 and ZQ71-HEP. After sectioning the bone specimens and staining with hematoxylin and eosin (HE) and Giemsa, we found that osteolytic destruction occurred in the cortical bone adjacent to the control and ZQ71 implants, where bone continuity was interrupted (Fig. S6). Bone destruction was accompanied by a progressive disappearance of the bone marrow with a large amount of inflammatory cell infiltration [11]. In contrast, the ZQ71-HEP group had better bone continuity around the implant and fewer inflammatory cells, suggesting that the construction of the $Mg(OH)_2$/GO/HA composite coating could significantly enhance the antibacterial activity of ZQ71 *in vivo* to hinder invasion of pathogenic bacteria [59,60].

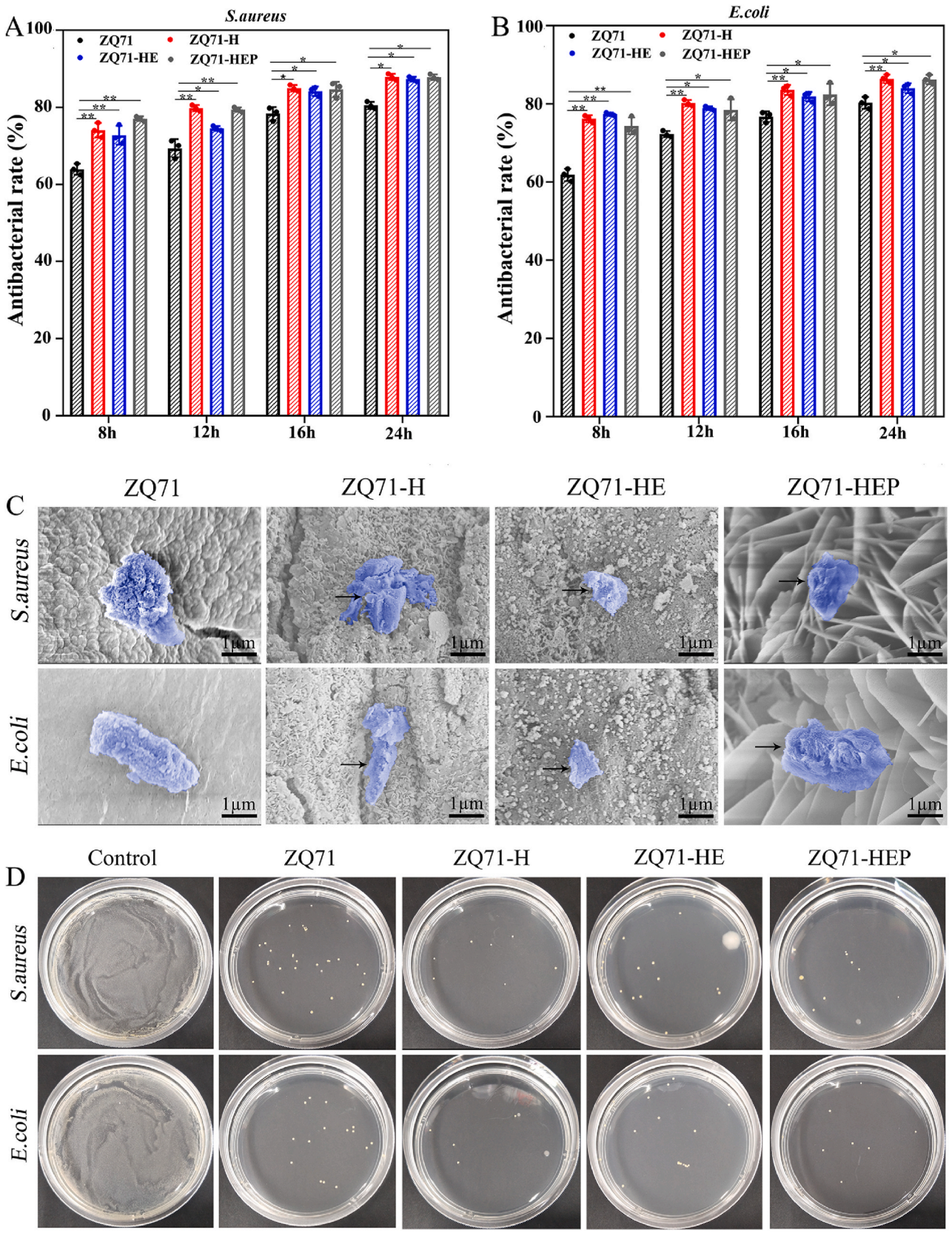

Fig. 5. *In vitro* antibacterial activity of various ZQ71 samples. The antibacterial rates of different samples against (A) *S. aureus* and (B) *E. coli*. (C) SEM images of bacteria on the surface of the ZQ71 samples after incubation at 37 °C for 12 h. (D) Culture of bacterial colonies on different samples. (*$p < 0.05$, **$p < 0.01$, ***$p < 0.001$).

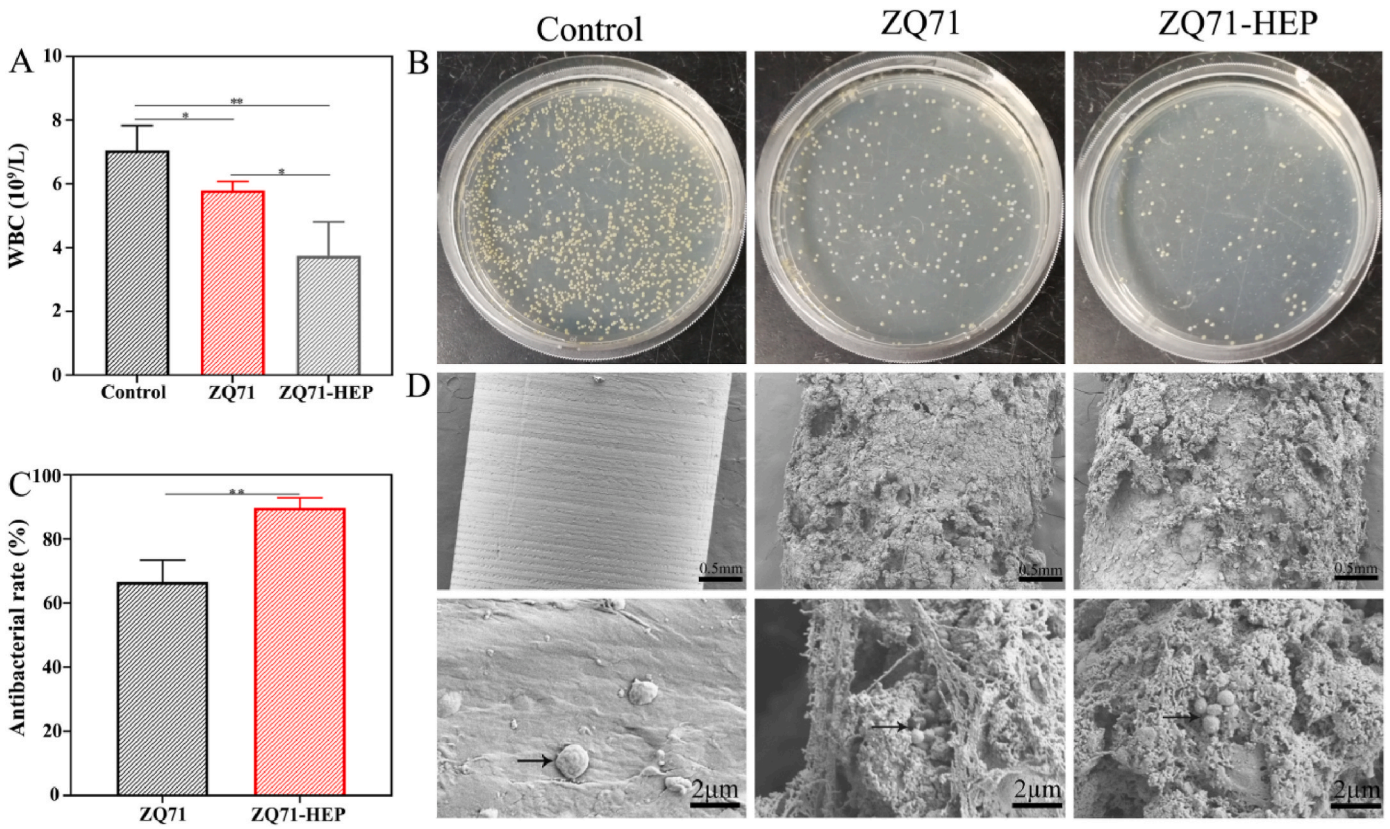

Fig. 6. *In vivo* antibacterial activity of various ZQ71 samples after implantation in a bacteria-infection model for 7 days. (A) White blood cell counts in the blood of the rats. (B) Images of *S. aureus* colonization on the surface of the ZQ71 implants by the spreading plate and (C) corresponding quantitative analysis results. (D) SEM observation on the residual bacteria colonized on the surface of the implants. (*$p < 0.05$, **$p < 0.01$, ***$p < 0.001$).

3.5. $Mg(OH)_2$/GO/HA nanocomposite coating showed an enhanced bone regeneration in both normal and bacterial conditions

To investigate the biological safety and bone regeneration ability of the surface-coated ZQ71 implant under normal and infected conditions, we first assessed the Mg^{2+} ions and bone turnover marker levels in serum after 4 weeks of implantation. As shown in Fig. S7A, no significant difference in serum Mg^{2+} ions was observed between the control and experimental groups under either normal or bacterial conditions, suggesting that the implantation of ZQ71 and ZQ71-HEP did not result in systemic changes in Mg^{2+} ionic concentrations in the rat serum. However, the serum levels of the bone formation marker PINP were significantly increased in the ZQ71-HEP group (Fig. S7B), suggesting an increased bone formation [61].

The regeneration of new bone and the degradation of implant materials were further visualized by a μ-CT image system. As shown in Fig. 7A, the cross-sectional view of metaphyseal bone in the defective region (red dotted line) showed that, under both normal and bacterial conditions, the ZQ71 implants (white) were degraded almost completely after 4 weeks of implantation, and only part of the spaces created by material degradation were substituted by the newly formed bone (gray). Similarly, a small amount of new bone formed within the defect area of the control group. In contrast, more new bone formation and less material degradation were found in the ZQ71-HEP group. It was worth noting that in the infection model, obvious bone destruction could be found in the cortical bone regions of the control and ZQ71 groups but not in the ZQ71-HEP group. According to the quantitative analysis of new bone shown in Fig. 7C, the BV/ΔMV of the ZQ71-HEP group in the normal model was 1.97- and 1.80-fold higher than that of the control and ZQ71 groups, respectively. Similarly, the BV/ΔMV of the ZQ71-HEP group in the infection model was 2.24- and 1.92-fold higher than that of the control and ZQ71 groups, respectively. In addition, the degradation rate of material in ZQ71 was much faster than that in ZQ71-HEP during the implantation period.

To verify the above μ-CT results, the implants retrieved at 4 weeks postoperatively was further analyzed by histological staining. As shown in Fig. 8A, the typical light microscopic image showed that a small amount of new bone formed within the defect areas of the control and ZQ71 groups in the normal models, and obvious bone destruction and osteolysis were observed in their bone infection models (Fig. 8B). This was mainly because bacteria under infection conditions secreted a variety of factors to elicit a host response consisting of the expression of various signaling molecules and mediators and the recruitment of inflammatory cells, which interfered with tissue regeneration and repaired and thus culminated in tissue destruction [62]. After implantation of ZQ71-HEP, the outermost HA coating with nano-scaled roughness and good hydrophilicity could inhibit initial bacterial adhesion by preventing the close contact of rigid cell wall of the bacteria with the coating surface [53,63] while promoting the spreading and differentiation of osteoblasts [64,65], which in turn prevented bacterial membrane formation and promoted new bone regeneration [66]. With the degradation of the HA coating, the residual bacteria colonizing the surface of the implant suffered mechanical tension from the $Mg(OH)_2$ and GO coatings and invasion of antibacterial ions (Mg^{2+}, Zn^{2+}, and Ag^{+}), resulting in membrane rupture and intracellular substance release [10,67]. Meanwhile, the released bioactive ions and degradation products from the composite coating stimulate extensive bone remodeling, leading to a good match between bone regeneration and material degradation [68,69]. Consequently, compared with control and ZQ71 groups, there was a significant improvement in osteolysis and impaired bone regeneration in ZQ71-HEP group, as confirmed by the increased bone substitution rate and osteogenic activity (Fig. 8C–F). Collectively, the results of *in vitro*

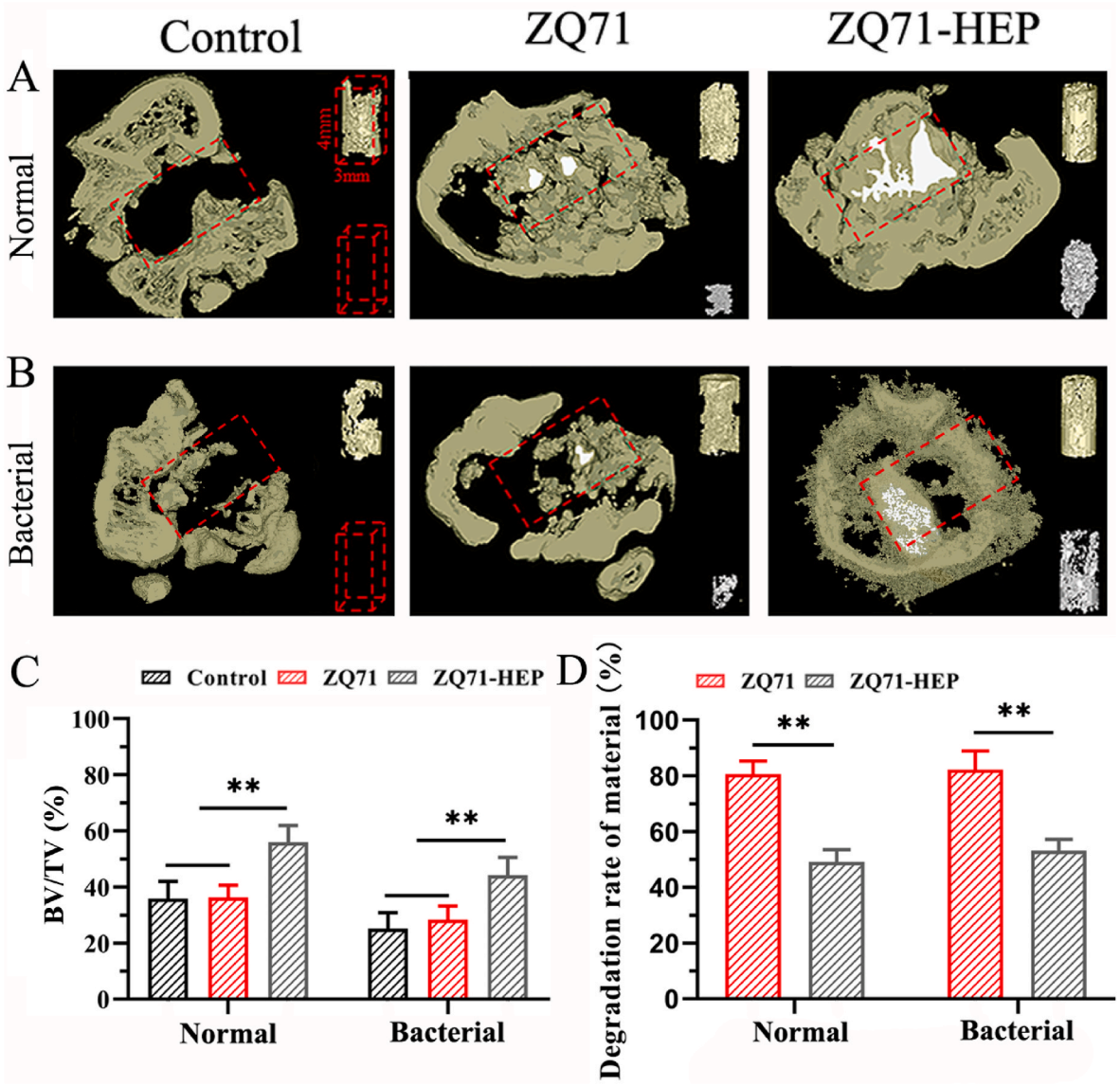

Fig. 7. μ-CT evaluation for the *in vivo* degradation and bone formation under normal and bacteria-infection conditions. Reconstructed micro-CT images of metaphyseal bone within the defective region (red dotted line) in (A) normal and (B) bacterial models at 4 weeks postoperatively. Upper right corner of each sample: the new bone formation within the defective region (gray). Bottom right corner of each sample: the residual alloy materials (white). (C) BV/TV: the percent volume of the newly formed bone (BV) relative to the total volume of the defect area. (D) The volume reduction rate of the implants: the percent volume of the degraded materials (ΔMV) relative to their paired initial volume (MV). (*$p < 0.05$, **$p < 0.01$, ***$p < 0.001$)

and *in vivo* experiments indicated that the construction of the Mg $(OH)_2$/GO/HA composite coating could synchronously slow Mg alloy degradation, kill pathogenic bacteria, and promote bone regeneration.

4. Conclusion

A $Mg(OH)_2$/GO/HA composite coating was successfully constructed on the surface of a ZQ71 alloy by the combination of hydrothermal treatment, electrophoretic deposition, and electrochemical deposition. The composite coating with high bonding strength and nanoscale topography significantly enhanced the corrosion resistance and reduced the degradation rate of ZQ71 alloy. *In vitro* cell culture using MC3T3-E1 cells demonstrated that the composite coating modified ZQ71 alloy (ZQ71-HEP) had higher cell viability and gene expression levels of osteogenic-related genes than ZQ71. In addition, enhanced antibacterial activity against both gram-positive bacteria (*S. aureus*) and gram-negative bacteria (*E. coli*) was observed on ZQ71-HEP. After implantation *in vivo*, compared to the ZQ71 and control groups, ZQ71-HEP displayed superior bactericidal effects and pro-osteogenesis in both the normal and infectious environments. Our findings provide an alternative for developing the multifunctional Mg-based implants, and enlarge the biomedical applications of Mg-based material.

CRediT authorship contribution statement

Bo Yuan: Methodology, Validation, Data curation, Writing – original draft, Funding acquisition. **Hewei Chen:** Methodology, Formal analysis, Data curation. **Rui Zhao:** Formal analysis. **Xuangeng Deng:** Conceptualization. **Guo Chen:** Conceptualization. **Xiao Yang:** Conceptualization, Formal analysis. **Zhanwen Xiao:** Methodology. **Antoniac Aurora:** Methodology. **Bita Ana Iulia:** Methodology. **Kai Zhang:** Writing – review & editing, Resources. **Xiangdong Zhu:** Writing – review & editing, Supervision, Resources, Funding acquisition. **Antoniac Vasile Iulian:** Conceptualization, Writing – review & editing, Funding acquisition. **Shen Hai:** Conceptualization, Resources. **Xingdong Zhang:** Conceptualization, Resources.

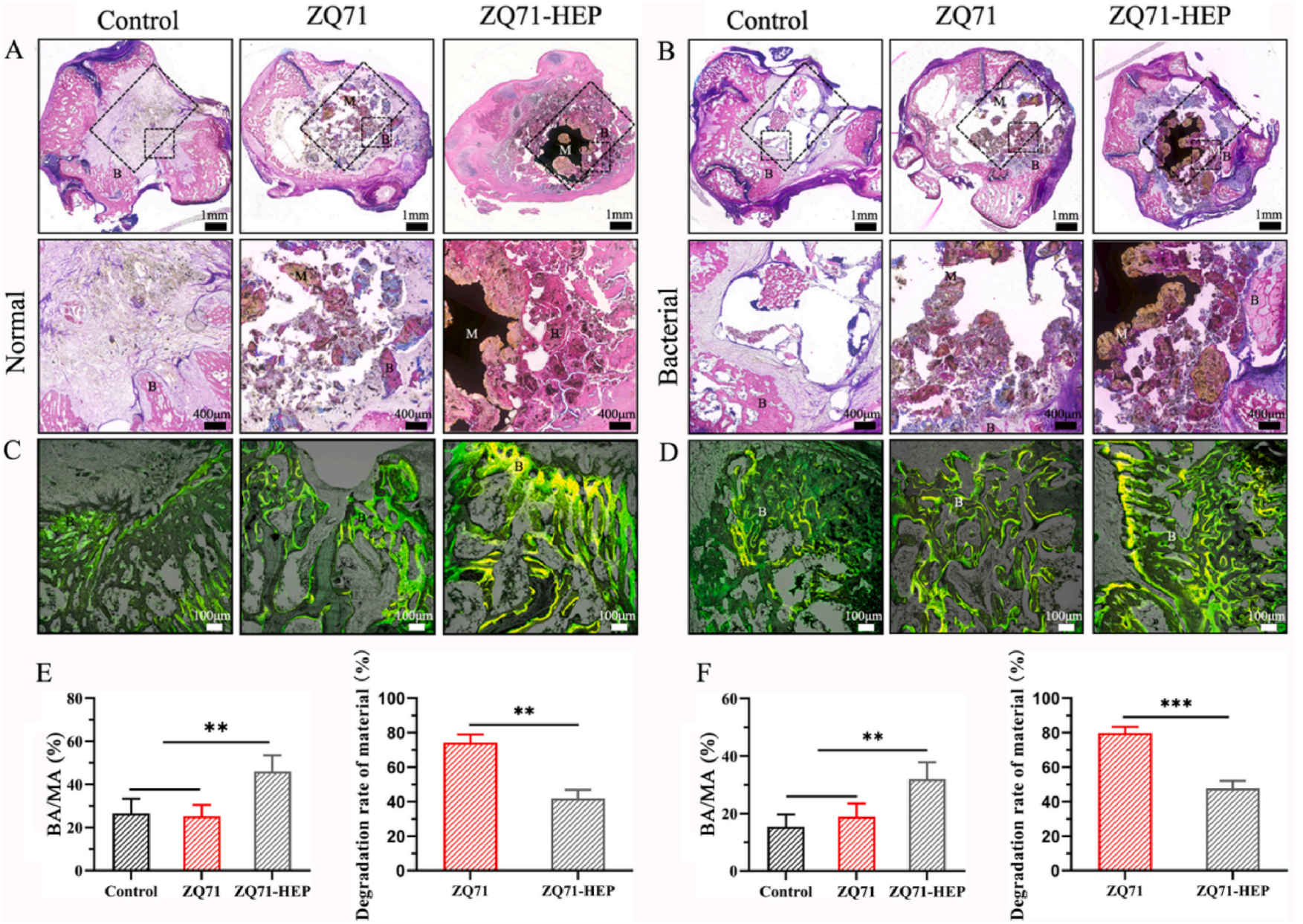

Fig. 8. Histological analysis for the bone regeneration under normal and bacteria-infection conditions. H&E staining of histological sections from different ZQ71 implants in (A) normal and (B) bacterial models at 4 weeks postoperatively. *in vivo* sequential fluorescent labeling of new bone formation in (C) normal and (D) bacterial models (Yellow: tetracycline label, Green: calcein label). The new bone substitution rates and the area reduction rate of the implants in (E) normal and (F) bacterial models. (B: bone tissue, M: material) (*$p < 0.05$, **$p < 0.01$, ***$p < 0.001$)

Declaration of competing interest

The authors declare that they have no known competing financial interests or personal relationships that could have appeared to influence the work reported in this paper.

Acknowledgements

This work was financially supported by Inter-Governmental S&T Cooperation Project Between China and Romania (2018LMNY003), Sichuan Science and Technology Program (2019JDTD0008, 2021YFS0020) and China Postdoctoral Science Foundation (2021M692316, 2020TQ0218).

Appendix A. Supplementary data

Supplementary data to this article can be found online at https://doi.org/10.1016/j.bioactmat.2022.02.030.

References

[1] F. Witte, The history of biodegradable magnesium implants: a review, Acta Biomater. 6 (2010) 1680–1692.
[2] D. Zhao, F. Witte, F. Lu, J. Wang, J. Li, L. Qin, Current status on clinical applications of magnesium-based orthopaedic implants: a review from clinical translational perspective, Biomaterials 112 (2017) 287–302.
[3] H. Zhou, B. Liang, H. Jiang, Z. Deng, K. Yu, Magnesium-based biomaterials as emerging agents for bone repair and regeneration: from mechanism to application, J. Magnes. Alloys 9 (2021) 779–804.
[4] J. Wang, Y. Wu, H. Li, Y. Liu, X. Bai, W. Chau, Y. Zheng, L. Qin, Magnesium alloy based interference screw developed for ACL reconstruction attenuates peri-tunnel bone loss in rabbits, Biomaterials 157 (2018) 86–97.
[5] J. Zhang, L. Tang, H. Qi, Q. Zhao, Y. Liu, Y. Zhang, Dual function of magnesium in bone biomineralization, Adv. Healthc. Mater. 8 (2019), e1901030.
[6] W. Qiao, K.H.M. Wong, J. Shen, W. Wang, J. Wu, J. Li, Z. Lin, Z. Chen, J. P. Matinlinna, Y. Zheng, S. Wu, X. Liu, K.P. Lai, Z. Chen, Y.W. Lam, K.M.C. Cheung, K.W.K. Yeung, TRPM7 kinase-mediated immunomodulation in macrophage plays a central role in magnesium ion-induced bone regeneration, Nat. Commun. 12 (2021) 2885.
[7] T.A. Grunewald, H. Rennhofer, B. Hesse, M. Burghammer, S.E. Stanzl-Tschegg, M. Cotte, J.F. Loffler, A.M. Weinberg, H.C. Lichtenegger, Magnesium from bioresorbable implants: distribution and impact on the nano- and mineral structure of bone, Biomaterials 76 (2016) 250–260.
[8] J.L. Wang, J.K. Xu, C. Hopkins, D.H. Chow, L. Qin, Biodegradable magnesium-based implants in orthopedics-A general review and perspectives, Adv. Sci. 7 (2020) 1902443.
[9] R. Hou, J. Victoria-Hernandez, P. Jiang, R. Willumeit-Romer, B. Luthringer-Feyerabend, S. Yi, D. Letzig, F. Feyerabend, In vitro evaluation of the ZX11 magnesium alloy as potential bone plate: degradability and mechanical integrity, Acta Biomater. 97 (2019) 608–622.
[10] Z. Lin, X. Sun, H. Yang, The role of antibacterial metallic elements in simultaneously improving the corrosion resistance and antibacterial activity of magnesium alloys, Mater. Des. 198 (2021).
[11] C.R. Arciola, D. Campoccia, L. Montanaro, Implant infections: adhesion, biofilm formation and immune evasion, Nat. Rev. Microbiol. 16 (2018) 397–409.
[12] H.R. Bakhsheshi-Rad, E. Hamzah, M. Daroonparvar, M.R. Abdul Kadir, M. Kasiri-Asgarani, M.P. Staiger, Enhancement of corrosion resistance and mechanical properties of Mg–1.2Ca–2Bi via a hybrid silicon-biopolymer coating system, Surf. Coating. Technol. 301 (2016) 133–139.
[13] S.L. Aktug, S. Durdu, S. Aktas, E. Yalcin, M. Usta, Surface and in vitro properties of Ag-deposited antibacterial and bioactive coatings on AZ31 Mg alloy, Surf. Coating. Technol. 375 (2019) 46–53.
[14] H.R. Bakhsheshi-Rad, A.F. Ismail, M. Aziz, M. Akbari, Z. Hadisi, M. Daroonparvar, X.B. Chen, Antibacterial activity and in vivo wound healing evaluation of polycaprolactone-gelatin methacryloyl-cephalexin electrospun nanofibrous, Mater. Lett. (2019) 256.
[15] Y. Husak, O. Solodovnyk, A. Yanovska, Y. Kozik, I. Liubchak, V. Ivchenko, O. Mishchenko, Y. Zinchenko, V. Kuznetsov, M. Pogorielov, Degradation and in vivo response of hydroxyapatite-coated Mg alloy, Coatings 8 (2018).
[16] H. Feng, G. Wang, W. Jin, X. Zhang, Y. Huang, A. Gao, H. Wu, G. Wu, P.K. Chu, Systematic study of inherent antibacterial properties of magnesium-based biomaterials, ACS Appl. Mater. Interfaces 8 (2016) 9662–9673.
[17] H. Chen, B. Yuan, R. Zhao, X. Yang, Z. Xiao, A. Aurora, B.A. Iulia, X. Zhu, A. V. Iulian, X. Zhang, Evaluation on the corrosion resistance, antibacterial property and osteogenic activity of biodegradable Mg-Ca and Mg-Ca-Zn-Ag alloys, J. Magnes. Alloys (2021), https://doi.org/10.1016/j.jma.2021.05.013.
[18] H.R. Bakhsheshi-Rad, E. Hamzah, A.F. Ismail, Z. Sharer, M.R. Abdul-Kadir, M. Daroonparvar, S.N. Saud, M. Medraj, Synthesis and corrosion behavior of a hybrid bioceramic-biopolymer coating on biodegradable Mg alloy for orthopaedic implants, J. Alloys Compd. 648 (2015) 1067–1071.
[19] A.I. Rezk, H.M. Mousa, J. Lee, C.H. Park, C.S. Kim, Composite PCL/HA/simvastatin electrospun nanofiber coating on biodegradable Mg alloy for orthopedic implant application, J. Coating Technol. Res. 16 (2018) 477–489.
[20] M. Razavi, M. Fathi, O. Savabi, D. Vashaee, L. Tayebi, In vitro study of nanostructured diopside coating on Mg alloy orthopedic implants, Mater. Sci. Eng. C Mater. Biol. Appl. 41 (2014) 168–177.
[21] S. Chen, P. Wan, B. Zhang, K. Yang, Y. Li, Facile fabrication of the zoledronate-incorporated coating on magnesium alloy for orthopaedic implants, J. Orthop. Translat. 22 (2020) 2–6.
[22] G. Wang, W. Jiang, S. Mo, L. Xie, Q. Liao, L. Hu, Q. Ruan, K. Tang, B. Mehrjou, M. Liu, L. Tong, H. Wang, J. Zhuang, G. Wu, P.K. Chu, Nonleaching antibacterial concept demonstrated by in situ construction of 2D nanoflakes on magnesium, Adv. Sci. 7 (2020) 1902089.
[23] Y. Dai, H. Guo, L. Chu, Z. He, M. Wang, S. Zhang, X. Shang, Promoting osteoblasts responses in vitro and improving osteointegration in vivo through bioactive coating of nanosilicon nitride on polyetheretherketone, J. Orthop. Translat. 24 (2020) 198–208.
[24] P. Wan, L. Tan, K. Yang, Surface modification on biodegradable magnesium alloys as orthopedic implant materials to improve the bio-adaptability: a review, J. Mater. Sci. Technol. 32 (2016) 827–834.
[25] K. Xie, L. Wang, Y. Guo, S. Zhao, Y. Yang, D. Dong, W. Ding, K. Dai, W. Gong, G. Yuan, Y. Hao, Effectiveness and safety of biodegradable Mg-Nd-Zn-Zr alloy screws for the treatment of medial malleolar fractures, J. Orthop. Translat. 27 (2021) 96–100.
[26] P. Tian, X. Liu, Surface modification of biodegradable magnesium and its alloys for biomedical applications, Regen. Biomater. 2 (2015) 135–151.
[27] S. Stankovich, D.A. Dikin, G.H. Dommett, K.M. Kohlhaas, E.J. Zimney, E.A. Stach, R.D. Piner, S.T. Nguyen, R.S. Ruoff, Graphene-based composite materials, Nature 442 (2006) 282–286.
[28] Y. Yang, Y. Cheng, S. Peng, L. Xu, C. He, F. Qi, M. Zhao, C. Shuai, Microstructure evolution and texture tailoring of reduced graphene oxide reinforced Zn scaffold, Bioact. Mater. 6 (2021) 1230–1241.
[29] C. Shuai, B. Wang, Y. Yang, S. Peng, C. Gao, 3D honeycomb nanostructure-encapsulated magnesium alloys with superior corrosion resistance and mechanical properties, Compos. B Eng. 162 (2019) 611–620.
[30] Y. Wu, Y. Wang, S. Tian, Y. Jing, J. Zhuang, L. Guo, D. Jia, Y. Zhou, Hydrothermal fabrication of rGO/Apatite layers on AZ31 magnesium alloy for enhanced bonding strength and corrosion resistance, Appl. Surf. Sci. 470 (2019) 430–438.
[31] J. Qiu, L. Liu, H. Zhu, X. Liu, Combination types between graphene oxide and substrate affect the antibacterial activity, Bioact. Mater. 3 (2018) 341–346.
[32] Y. Zeng, M. Zhou, L. Chen, H. Fang, S. Liu, C. Zhou, J. Sun, Z. Wang, Alendronate loaded graphene oxide functionalized collagen sponge for the dual effects of osteogenesis and anti-osteoclastogenesis in osteoporotic rats, Bioact. Mater. 5 (2020) 859–870.
[33] Z. Yang, Y. Xi, J. Bai, Z. Jiang, S. Wang, H. Zhang, W. Dai, C. Chen, Z. Gou, G. Yang, C. Gao, Covalent grafting of hyperbranched poly-L-lysine on Ti-based implants achieves dual functions of antibacteria and promoted osteointegration in vivo, Biomaterials 269 (2021) 120534.
[34] B. Yuan, L. Wang, R. Zhao, X. Yang, X. Yang, X. Zhu, L. Liu, K. Zhang, Y. Song, X. Zhang, A biomimetically hierarchical polyetherketoneketone scaffold for osteoporotic bone repair, Sci. Adv. 6 (2020), eabc4704.
[35] E.V. Alakpa, K.E.V. Burgess, P. Chung, M.O. Riehle, N. Gadegaard, M.J. Dalby, M. Cusack, Nacre topography produces higher crystallinity in bone than chemically induced osteogenesis, ACS Nano 11 (2017) 6717–6727.
[36] J. Z, Z. K, Effect of different liquid–solid contact models on the corrosion resistance of superhydrophobic magnesium surfaces, Corrosion Sci. 87 (2014) 452–459.
[37] Q. Jin, G. Tian, J. Li, Y. Zhao, H. Yan, The study on corrosion resistance of superhydrophobic magnesium hydroxide coating on AZ31B magnesium alloy, Colloids Surf. A Physicochem. Eng. Asp. 577 (2019) 8–16.
[38] C. Wen, X. Zhan, X. Huang, F. Xu, L. Luo, C. Xia, Characterization and corrosion properties of hydroxyapatite/graphene oxide bio-composite coating on magnesium alloy by one-step micro-arc oxidation method, Surf. Coating. Technol. 317 (2017) 125–133.
[39] X. Ma, S. Zhu, L. Wang, C. Ji, C. Ren, S. Guan, Synthesis and properties of a bio-composite coating formed on magnesium alloy by one-step method of micro-arc oxidation, J. Alloys Compd. 590 (2014) 247–253.
[40] B. Yuan, Q. Cheng, R. Zhao, X. Zhu, X. Yang, X. Yang, K. Zhang, Y. Song, X. Zhang, Comparison of osteointegration property between PEKK and PEEK: effects of surface structure and chemistry, Biomaterials 170 (2018) 116–126.
[41] N.J. Shah, M.N. Hyder, J.S. Moskowitz, M.A. Quadir, S.W. Morton, H. J. Seeherman, R.F. Padera, M. Spector, P.T. Hammond, Surface-mediated bone tissue morphogenesis from tunable nanolayered implant coatings, Sci. Transl. Med. 5 (2013) 191ra83.
[42] M. Aparicio, J. Mosa, G. Rodriguez, J. Guzman, Q. Picard, L.C. Klein, A. Jitianu, Consolidated melting gel coatings on AZ31 magnesium alloy with excellent corrosion resistance in NaCl solutions: an interface study, ACS Appl. Mater. Interfaces 11 (2019) 3493–3505.
[43] M.S. Kabir, P. Munroe, Z. Zhou, Z. Xie, Scratch adhesion and tribological behaviour of graded Cr/CrN/CrTiN coatings synthesized by closed-field unbalanced magnetron sputtering, Wear 380–381 (2017) 163–175.
[44] H. Farnoush, J. Aghazadeh Mohandesi, H. Cimenoglu, Micro-scratch and corrosion behavior of functionally graded HA-TiO2 nanostructured composite coatings fabricated by electrophoretic deposition, J. Mech. Behav. Biomed. Mater. 46 (2015) 31–40.

[45] J. Forsgren, F. Svahn, T. Jarmar, H. Engqvist, Formation and adhesion of biomimetic hydroxyapatite deposited on titanium substrates, Acta Biomater. 3 (2007) 980–984.
[46] X. Zhou, X. Fu, H. Chen, Z. Xiao, L. Min, Y. Zhou, X. Zhu, K. Zhang, C. Tu, X. Zhang, Evaluation and regulation of the corrosion resistance of macroporous titanium scaffolds with bioactive surface films for biomedical applications, J. Mater. Chem. B 7 (2019) 3455–3467.
[47] D. T, R. H, K. A, A novel modification of an alkanethiol self-assembled monolayer with alkylisocyanates to prepare protective films against copper corrosion, Corrosion Sci. 43 (2001) 1589–1600.
[48] S. Huang, B. Wang, X. Zhang, F. Lu, Z. Wang, S. Tian, D. Li, J. Yang, F. Cao, L. Cheng, Z. Gao, Y. Li, K. Qin, D. Zhao, High-purity weight-bearing magnesium screw: translational application in the healing of femoral neck fracture, Biomaterials 238 (2020) 119829.
[49] J.W. Lee, H.S. Han, K.J. Han, J. Park, H. Jeon, M.R. Ok, H.K. Seok, J.P. Ahn, K. E. Lee, D.H. Lee, S.J. Yang, S.Y. Cho, P.R. Cha, H. Kwon, T.H. Nam, J.H. Han, H. J. Rho, K.S. Lee, Y.C. Kim, D. Mantovani, Long-term clinical study and multiscale analysis of in vivo biodegradation mechanism of Mg alloy, Proc. Natl. Acad. Sci. Unit. States Am. 113 (2016) 716–721.
[50] P. Mora-Raimundo, D. Lozano, M. Manzano, M. Vallet-Regi, Nanoparticles to knockdown osteoporosis-related gene and promote osteogenic marker expression for osteoporosis treatment, ACS Nano 13 (2019) 5451–5464.
[51] K. Zhou, P. Yu, X. Shi, T. Ling, W. Zeng, A. Chen, W. Yang, Z. Zhou, Hierarchically porous hydroxyapatite hybrid scaffold incorporated with reduced graphene oxide for rapid bone ingrowth and repair, ACS Nano 13 (2019) 9595–9606.
[52] S. Liu, T.H. Zeng, M. Hofmann, E. Burcombe, J. Wei, R. Jiang, Jing Kong, Y. Chen, Antibacterial activity of graphite, graphite oxide, graphene oxide, and reduced graphene oxide membrane and oxidative stress, ACS Nano 5 (2011) 6971–6980.
[53] J.T. Seil, T.J. Webster, Antimicrobial applications of nanotechnology: methods and literature, Int. J. Nanomed. 7 (2012) 2767–2781.
[54] A. Singh, A.K. Dubey, Various biomaterials and techniques for improving antibacterial response, ACS Appl. Bio Mater. 1 (2018) 3–20.
[55] H. Chouirfa, H. Bouloussa, V. Migonney, C. Falentin-Daudre, Review of titanium surface modification techniques and coatings for antibacterial applications, Acta Biomater. 83 (2019) 37–54.
[56] P.H. Chua, K.G. Neoh, Z. Shi, E.T. Kang, Structural stability and bioapplicability assessment of hyaluronic acid-chitosan polyelectrolyte multilayers on titanium substrates, J. Biomed. Mater. Res. 87 (2008) 1061–1074.
[57] P. Singha, J. Pant, M.J. Goudie, C.D. Workman, H. Handa, Enhanced antibacterial efficacy of nitric oxide releasing thermoplastic polyurethanes with antifouling hydrophilic topcoats, Biomater. Sci. 5 (2017) 1246–1255.
[58] D. Wolf, N. Anto-Michel, H. Blankenbach, A. Wiedemann, K. Buscher, J. D. Hohmann, B. Lim, M. Bauml, A. Marki, M. Mauler, D. Duerschmied, Z. Fan, H. Winkels, D. Sidler, P. Diehl, D.M. Zajonc, I. Hilgendorf, P. Stachon, T. Marchini, F. Willecke, M. Schell, B. Sommer, C. von Zur Muhlen, J. Reinohl, T. Gerhardt, E. F. Plow, V. Yakubenko, P. Libby, C. Bode, K. Ley, K. Peter, A. Zirlik, A ligand-specific blockade of the integrin Mac-1 selectively targets pathologic inflammation while maintaining protective host-defense, Nat. Commun. 9 (2018) 525.
[59] Z. Lin, Y. Zhao, P.K. Chu, L. Wang, H. Pan, Y. Zheng, S. Wu, X. Liu, K.M.C. Cheung, T. Wong, K.W.K. Yeung, A functionalized TiO2/Mg2TiO4 nano-layer on biodegradable magnesium implant enables superior bone-implant integration and bacterial disinfection, Biomaterials 219 (2019) 119372.
[60] Z. Lin, S. Wu, X. Liu, S. Qian, P.K. Chu, Y. Zheng, K.M.C. Cheung, Y. Zhao, K.W. K. Yeung, A surface-engineered multifunctional TiO2 based nano-layer simultaneously elevates the corrosion resistance, osteoconductivity and antimicrobial property of a magnesium alloy, Acta Biomater. 99 (2019) 495–513.
[61] Z. Liu, X. Yao, G. Yan, Y. Xu, J. Yan, W. Zou, G. Wang, Mediator MED23 cooperates with RUNX2 to drive osteoblast differentiation and bone development, Nat. Commun. 7 (2016) 11149.
[62] M.V. Thomas, D.A. Puleo, Infection, inflammation, and bone regeneration: a paradoxical relationship, J. Dent. Res. 90 (2011) 1052–1061.
[63] G. Bhardwaj, H. Yazici, T.J. Webster, Reducing bacteria and macrophage density on nanophase hydroxyapatite coated onto titanium surfaces without releasing pharmaceutical agents, Nanoscale 7 (2015) 8416–8427.
[64] N. Zhang, W. Wang, X. Zhang, K.C. Nune, Y. Zhao, N. Liu, R.D.K. Misra, K. Yang, L. Tan, J. Yan, The effect of different coatings on bone response and degradation behavior of porous magnesium-strontium devices in segmental defect regeneration, Bioact. Mater. 6 (2021) 1765–1776.
[65] T.J. Dennes, J. Schwartz, A nanoscale Adhesion layer to promote cell attachment on PEEK, J. Am. Chem. Soc. 131 (2009) 3456–3457.
[66] R.A. Gittens, L. Scheideler, F. Rupp, S.L. Hyzy, J. Geis-Gerstorfer, Z. Schwartz, B. D. Boyan, A review on the wettability of dental implant surfaces II: biological and clinical aspects, Acta Biomater. 10 (2014) 2907–2918.
[67] Y. Li, L. Liu, P. Wan, Z. Zhai, Z. Mao, Z. Ouyang, D. Yu, Q. Sun, L. Tan, L. Ren, Z. Zhu, Y. Hao, X. Qu, K. Yang, K. Dai, Biodegradable Mg-Cu alloy implants with antibacterial activity for the treatment of osteomyelitis: in vitro and in vivo evaluations, Biomaterials 106 (2016) 250–263.
[68] D.E. Place, R.K.S. Malireddi, J. Kim, P. Vogel, M. Yamamoto, T.D. Kanneganti, Osteoclast fusion and bone loss are restricted by interferon inducible guanylate binding proteins, Nat. Commun. 12 (2021) 496.
[69] Y.H. Zou, J. Wang, L.Y. Cui, R.C. Zeng, Q.Z. Wang, Q.X. Han, J. Qiu, X.B. Chen, D. C. Chen, S.K. Guan, Y.F. Zheng, Corrosion resistance and antibacterial activity of zinc-loaded montmorillonite coatings on biodegradable magnesium alloy AZ31, Acta Biomater. 98 (2019) 196–214.